Broadband integrated racetrack ring resonators for long-wave infrared photonics

Joan Manel Ramirez,[1,*] Qiankun Liu,[1,†] Vladyslav Vakarin,[1,†] Xavier Le Roux,[1] Jacopo Frigerio,[2] Andrea Ballabio,[2] Carlos Alonso-Ramos,[1] Enrico Talamas Simola,[2] Laurent Vivien,[1] Giovanni Isella,[2] and Delphine Marris-Morini[1]

[1]Centre de Nanosciences et de Nanotechnologies (C2N), Université Paris Sud, CNRS, Université Paris Saclay, 91405 Orsay, France
[2]L-NESS, Dipartimento di Fisica, Politecnico di Milano, Polo di Como, Via Anzani 42, 22100 Como, Italy
*Corresponding author: joan.ramirez@3-5lab.fr

Long-wave infrared photonics is an exciting research field meant to revolutionize our daily life by means of key advances in several domains including communications, imaging systems, medical care, environmental monitoring, or multispectral chemical sensing, among others. For this purpose, integrated photonics is particularly promising owing to its compactness, mass fabrication, and energy-efficient characteristics. We present in this Letter, for the first time to the best of our knowledge, broadband integrated racetrack ring resonators operating within the crucial molecular fingerprint region. Devices show an operation bandwidth of $\Delta\lambda \approx 900$ nm with a central wavelength of $\lambda \approx 8$ μm, a quality factor of $Q \approx 3200$, and an extinction ratio of ER ≈ 10 dB around the critical coupling condition. These resonant structures establish the basis of a new generation of integrated building blocks for long-wave infrared photonics that opens the route towards miniaturized multi-target molecule detection systems. © 2019 Optical Society of America

Mid-infrared (mid-IR) photonics is becoming an interesting research field due to the wide plethora of applications foreseen in different arenas of our society, including high-resolution biosensing, early medical diagnosis, security, free-space optical communications, defense, 3D imaging, and many more [1–3]. Among them, the identification of molecules via vibrational spectroscopy in the long-wave infrared (LWIR) range using photonic integrated circuits (PICs) has been a subject of intense research due to the expected superior performance compared to other existing approaches [4]. In this regard, silicon (Si) photonics is expected to have a high impact in mid-IR photonics. Indeed, Si photonics provides a reliable and high-volume platform that leverages from a mature technology that has been largely employed by now to develop solutions in the near-IR wavelength range, notably for telecom/datacom applications [5]. However, the extension of the operation wavelength range of conventional silicon-on-insulator (SOI) waveguides towards the mid-IR is not straightforward due to the optical absorption of the buried SiO_2 layer for wavelengths beyond $\lambda = 3.6$ μm. Different approaches have been proposed to extend Si photonics towards the mid-IR, including the implementation of waveguide engineering strategies to minimize the mode overlap with the bottom cladding [6], the use of pedestal waveguides [7], or the development of suspended membranes [8,9]. While these approaches can be successful below an 8 μm wavelength, according to the Si mid-IR transparency window, alternative solutions are required to exploit larger mid-IR wavelengths. For this purpose, germanium (Ge) stands as a promising material owing to its extended transparency up to $\lambda = 15$ μm, its complementary metal-oxide semiconductor (CMOS) technology maturity, its high third-order nonlinearity, and its large refractive index that makes it suitable to implement compact integrated devices with a small footprint. Therefore, GE-on-Si has been often chosen as a platform to implement LWIR PICs, as it can operate over a wide wavelength range within the molecular fingerprint region (5 μm $< \lambda <$ 12 μm) with low/moderate propagation loss [10–13]. Similarly, graded silicon–germanium (SiGe) has also been employed as an enabling integrated platform, as it permits a gradual accommodation of the lattice mismatch between Si and Ge, hence obtaining a Ge-rich SiGe epilayer with good crystalline quality and low defect density [14]. Thus, graded-index SiGe alloys benefit from the advantages of Ge while providing high versatility in terms of mode confinement, as their optical properties can be effectively controlled by careful engineering of the vertical refractive index profile [15]. Recently, we have demonstrated several broadband LWIR photonic components and building blocks using the graded-index SiGe platform, including low-loss and polarization-insensitive waveguides [16,17], Mach–Zehnder interferometers [18], dual-polarization Fourier Transform spectrometers [19], or Bragg grating Fabry–Perot cavities [20].

A preliminary LWIR sensing proof-of-concept has also been realized between 5.2 μm and 6.6 μm wavelengths [21]. In this context, the implementation of microring resonators appears interesting, as it has many utilities in integrated photonics,

such as its implementation as (i) a notch filter to finely select and reject narrow frequency bands, (ii) a compact sensor that effectively increases the interaction length between the propagating mode and the analyte, (iii) an elementary unit for optical delay lines, (iv) an efficient modulator, or (v) a nonlinear device, which provides a strong light–matter interaction with the non-linear material to generate frequency combs around the pumping wavelength [22]. Current development of LWIR ring resonators is still in its infancy, with demonstrations that cover a wavelength span of $\lambda = 2.75$–5.6 µm [23–26], a range that remains insufficient for the envisioned applications of LWIR-integrated platforms [27]. It is worth noting that extending the operation range of ring resonators well into the LWIR wavelength range is not trivial, as the use of Ge-based integrated platforms with a relatively low index contrast could compromise the compactness of the ring resonator and ultimately the maximum free-spectral range (FSR) attainable. In the following, we will show that by a careful design of the resonators, LWIR-integrated racetrack ring resonators can be implemented.

In this Letter, we demonstrate for the first time, to the best of our knowledge, an integrated LWIR racetrack ring resonator implemented on a Ge-rich SiGe material platform that works at LWIR wavelengths around $\lambda \approx 8$ µm, shows a maximum loaded quality factor (Q) of 3200, and offers a high LWIR bandwidth ($\Delta\lambda$) of 900 nm and a maximum extinction ratio (ER) of 10 dB. These results demonstrate that integrated long-wave resonant structures are feasible using Ge-rich graded-index SiGe layers, opening up the way towards advanced LWIR PICs.

Racetrack ring resonators were developed in a 6 µm thick graded-index SiGe layer grown by low-energy plasma-enhanced chemical vapor deposition (LEPECVD) [28]. A linear increase of the Ge concentration along the growth direction from Si up to pure Ge is used to confine light on the upper part of the waveguide. Waveguides are then designed using a rib-like geometry with an etching depth of 3 µm and a width of 4 µm. Further details of this platform can be found elsewhere [29]. Racetrack resonators were designed to operate at $\lambda \approx 8$ µm, taking into account several requirements. First, the directional couplers have to provide a power coupling factor (k^2) able to compensate for one round trip loss in the resonator. The gap distance (g) and coupling length (L) have then been chosen as $g = 1$ µm and $L = 200$ µm to ease the fabrication process keeping reasonable aspect ratio for the gap definition, while maintaining a compact device footprint and a FSR above the minimum wavelength resolution of the experimental setup, i.e., larger than 1 cm^{-1}. Figure 1 shows an example of simulation of the E_y component of the even [Fig. 1(a)] and odd [Fig. 1(b)] quasi-TM supermodes in the directional coupler. The power coupling factor was deduced for a coupling length of $L = 200$ µm, as reported in Fig. 1(c). Interestingly, the achieved value, $k^2 \approx 0.2$, is compatible with the propagation loss in the resonator cavity of a few dB/cm. A remarkable flat profile of k^2 from 7.5 to 8.5 µm is observed, with a moderate linear increase from $k^2 = 0.1$ ($\lambda = 7.5$ µm) to $k^2 = 0.35$ ($\lambda = 8.5$ µm), denoting the ability of these directional couplers to operate over a broadband at LWIR wavelengths. This phenomenon is attributed to the particular combination of a low material dispersion at these wavelengths and the propagating mode readaptation induced by the vertical graded-index profile [15].
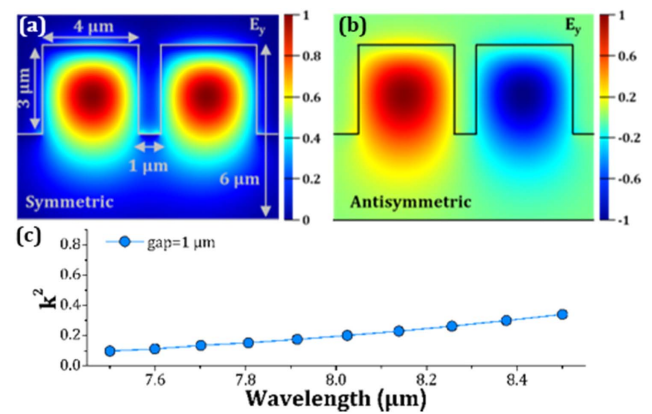

Fig. 1. (a) Even and (b) odd quasi-TM guided supermodes of the directional coupler containing graded-index SiGe waveguides. Waveguide width is 4 µm, the etching depth is 3 µm, and the gap between the waveguides is 1 µm. (c) Simulated power coupling factor, k^2, for a coupling length of $L = 200$ µm from $\lambda = 7.5$ µm to 8.5 µm.

Similarly, the bending radius of racetrack ring resonators was chosen considering the trade-off between the reduction of the round trip loss (by increasing the bending radius) and the minimum FSR value imposed by our experimental setup. Based on these considerations, and taking into account previously reported propagation losses of 2–3 dB/cm [29], five different bending radiuses between $R = 50$ µm and $R = 250$ µm were selected.

Racetrack ring resonators were fabricated using e-beam lithography followed by a selective induced coupled plasma (ICP) etching. Figure 2(a) presents a cross section scanning electron microscopy (SEM) image of the coupling region of a test resonant structure. A top SEM view of a racetrack ring resonator with $R = 100$ µm is shown in Fig. 2(b). After fabrication, waveguide facets were diced to facilitate butt-coupling of the free-space laser beam. Devices were characterized using
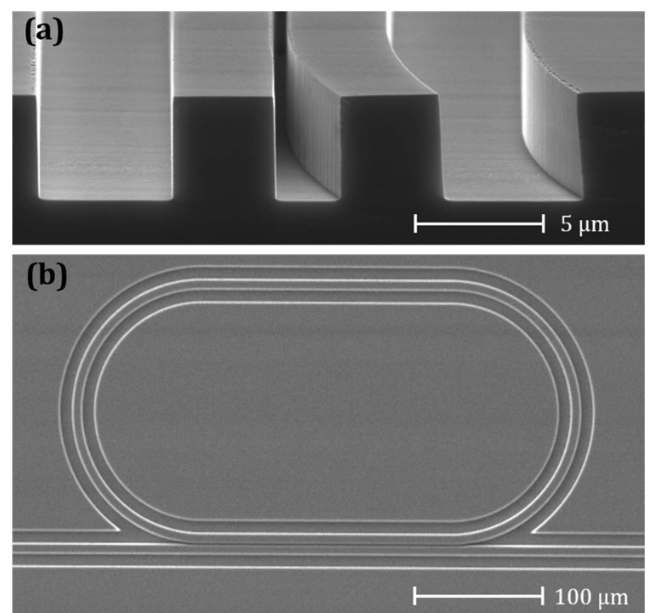

Fig. 2. (a) Cross section SEM view of a test resonator device in the coupling area. (b) Top SEM view of a racetrack ring resonator.

an external cavity quantum cascade laser operating in quasi-TM polarization and in pulsed regime (duty cycle of 5% and repetition rate of 100 kHz), with a linewidth specified to be below 1 cm^{-1}. A wavelength range from $\lambda = 7.5$ μm (1333.3 cm^{-1}) to 8.6 μm (1162.8 cm^{-1}) was investigated.

The input/output signals were coupled in and out of the chip by means of ZnSe aspheric lenses, obtaining a typical coupling loss of 4 dB/facet. The collected signal was sent through either a high-resolution camera to visualize the spatial profile of the propagating mode or to a HgCdTe (MCT) detector to scan the transmission spectrum.

Figure 3 summarizes the normalized quasi-TM transmission of the racetrack ring resonators with increasing radius of curvature in a bottom-up arrangement. The characteristic interferometric pattern of ring resonators is observed, presenting periodic transmission dips that are sometimes partially clipped due to the limited resolution of our setup. Noticeably, the lowest radius of curvature, i.e., $R = 50$ μm, shows a poor performance with resonance patterns of 4 dB in average and a multimode-like spectrum that deforms the transmission curve. This fact can be attributed to a partial hybridization of the modes, obtaining a non-negligible conversion of the fundamental quasi-TM mode

into quasi-TE polarization (in agreement with finite element method (FEM) simulations). Furthermore, a remarkably higher bending loss is to be expected compared to other structures, hence shifting the critical coupling condition to gap values lower than 1 μm. Asymmetric resonances are also observed for the resonator having an $R = 100$ μm, which is equally attributed to a mode hybridization effect, although much weaker. Moreover, it is worth noting the superimposed modulation of the interferometric pattern causes oscillations of the resonance depth, which are typically attributed to the oscillatory behavior of the transmitted signal in the directional couplers [30].

Concerning the transmittance response, resonators with $R > 50$ μm display deep resonances with an ER up to 10 dB. Figure 3(b) shows a zoomed-in view of a resonance corresponding to the biggest racetrack resonator ($R = 250$ μm). A Lorentzian fit is used to extract the full width at half-maximum (FWHM), which will ultimately be used to extract the loaded quality factor,

$$Q = \frac{\lambda_{\text{central}}}{\text{FWHM}}. \tag{1}$$

A maximum loaded quality factor of $Q \approx 3200$ is measured at $\lambda \approx 8.044$ μm, which corresponds to a FWHM of 0.38 cm^{-1}. When compared to the laser linewidth used in the experiment (<1 cm^{-1} from the specification) we can deduce that the measured resonance spectral shape and Q-factor are most probably limited by the experimental setup. Interestingly, the critical coupling wavelength (around of 8.1–8.2 μm) is compatible with a waveguide propagation loss of 3 dB/cm and negligible bend loss for $R > 150$ μm [29].

In order to further verify the fundamental mode operation of the devices for $R > 50$ μm, the FSR of the resonances was measured as a function of the wavelength and compared with the theoretical model, assuming the following equation:

$$\text{FSR} = \frac{\lambda^2}{n_g L}, \tag{2}$$

where n_g is the group refractive index of the propagating mode, λ is the operating wavelength, and L is the round trip length. Figure 4 presents the dispersion of the FSR for each bending
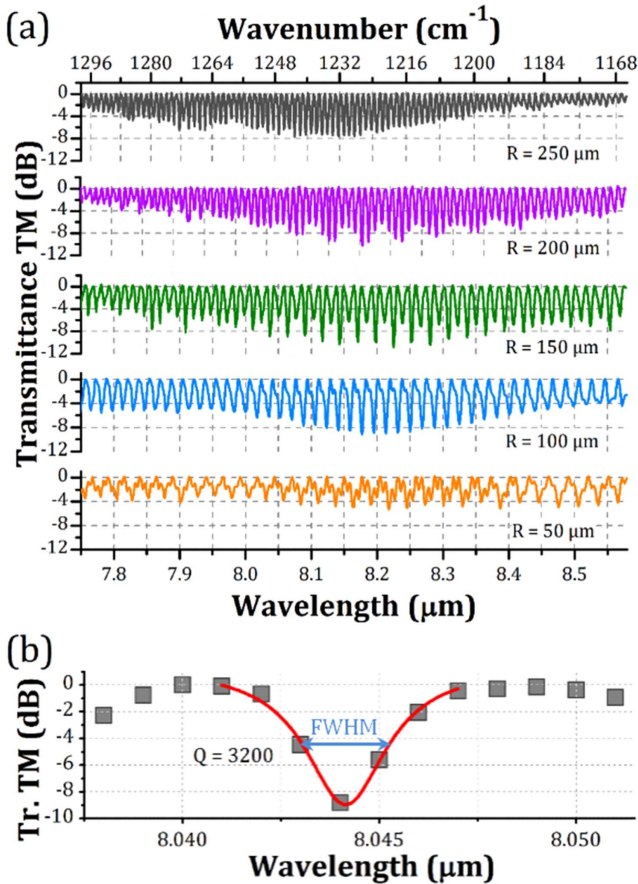

Fig. 3. (a) Experimental transmission spectra of racetrack ring resonators operating in quasi-TM polarization and arranged according to increasing bending radius. From the bottom up, $R = 50$ μm (orange curve), $R = 100$ μm (light blue), $R = 150$ μm (green), $R = 200$ μm (violet), and $R = 250$ μm (gray curve). (b) Zoomed-in view of a single resonance (gray squares), corresponding to a resonator with $R = 250$ μm, showing a Lorentzian fit (red curve) and a calculated quality factor of $Q = 3200$.

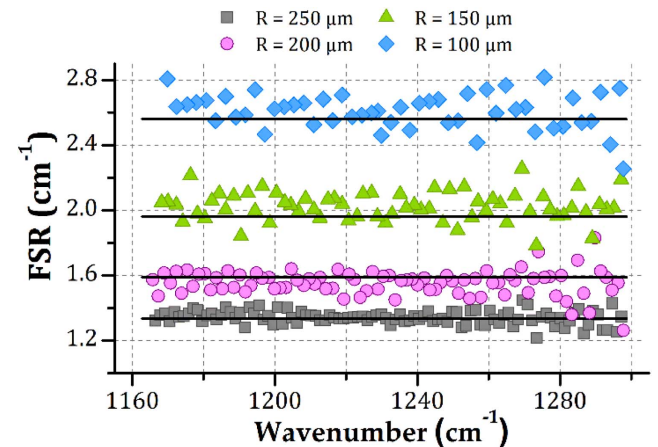**Fig. 4.** Measured FSR values as a function of wavelength and the bending radius, being the gray squares $R = 250$ μm, the light pink dots $R = 200$ μm, the green triangles $R = 150$ μm, and the light blue lozenges $R = 100$ μm. Straight black lines correspond to the expected spectral response according to Eq. (1) for $n_g = 3.8$.

radius, with the theoretical model of Eq. (2) superimposed, assuming $n_g = 3.8$. As seen, bigger FSR values were measured for the lower bending radius, as expected. Moreover, good agreement between the experimental results and the modeling was found, providing evidence that the observed resonances correspond to a single propagating mode inside racetrack ring resonators.

In conclusion, we have shown, to the best of our knowledge, the first demonstration of broadband integrated racetrack ring resonators for LWIR photonics that operate around 8 µm wavelength. The resonant structures have been implemented using a 6 µm thick Ge-rich graded-index SiGe platform that contains a linear increase of the Ge concentration in the vertical direction. Devices show a bandwidth of $\Delta\lambda \approx 900$ nm, a maximum quality factor of $Q = 3200$, and an ER of 10 dB around the critical coupling condition. This work paves the way towards the implementation of multitarget molecular spectroscopic sensors in integrated photonic platforms.

†These authors contributed equally to this work.

REFERENCES

1. R. Soref, Nat. Photonics **4**, 495 (2010).
2. J. Haas and B. Mizaikoff, Annu. Rev. Anal. Chem. **9**, 45 (2016).
3. X. Wang, S. S. Kim, R. Roßbach, M. Jetter, P. Michler, and B. Mizaikoff, Analyst **137**, 2322 (2012).
4. Y. Chen, H. Lin, J. Hu, and M. Li, ACS Nano **8**, 6955 (2014).
5. R. Soref, IEEE J. Sel. Top. Quantum Electron. **12**, 1678 (2006).
6. S.-A. Miller, M. Yu, X. Ji, G. Griffith, J. Cardenas, A.-L. Gaeta, and M. Lipson, Optica **4**, 707 (2017).
7. P.-T. Lin, V. Singh, J. Hu, K. Richardson, J.-D. Musgraves, I. Luzinov, J. Hensley, L.-C. Kimerling, and A. Agarwal, Lab Chip **13**, 2161 (2013).
8. M. Nedeljkovic, A. Z. Khokhar, Y. Hu, X. Chen, J. Soler Penades, and S. Stankovic, Opt. Mater. Express **3**, 1205 (2013).
9. J. Soler Penadés, C. Alonso-Ramos, A. Z. Khokhar, M. Nedeljkovic, A. Ortega-Moñux, I. Molina-Fernández, P. Cheben, and G. Z. Mashanovich, Opt. Lett. **39**, 5661 (2014).
10. D. Marris-Morini, V. Vakarin, J. M. Ramirez, Q. Liu, A. Ballabio, J. Frigerio, M. Montesinos, C. Alonso-Ramos, X. Le Roux, S. Serna, D. Benedikovic, D. Chrastina, L. Vivien, and G. Isella, Nanophotonics **7**, 1781 (2018).
11. M. Muneeb, X. Chen, P. Verheyen, G. Lepage, S. Pathak, E. Ryckeboer, A. Malik, B. Kuyken, M. Nedeljkovic, J. Van Campenhout, and G. Mashanovich, Opt. Express **21**, 11659 (2013).
12. Z. Lin, A. M. Agarwal, L. C. Kimerling, and J. Michel, Nanophotonics **3**, 247 (2014).
13. T.-H. Xiao, Z. Ziqiang, Z. Wen, T. Mitsuru, K. T. Hon, C. Zhenzhou, and G. Keisuke, Opt. Lett. **42**, 2882 (2017).
14. S. Marchionna, A. Virtuani, M. Acciarri, G. Isella, and H. von Kaenel, Mater. Sci. Semicond. Process. **9**, 802 (2006).
15. J. M. Ramirez, V. Vakarin, J. Frigerio, P. Chaisakul, D. Chrastina, X. Le Roux, A. Ballabio, L. Vivien, G. Isella, and D. Marris-Morini, Opt. Express **25**, 6561 (2017).
16. J. M. Ramirez, V. Vakarin, C. Gilles, J. Frigerio, A. Ballabio, P. Chaisakul, X. Le Roux, C. Alonso-Ramos, G. Maisons, L. Vivien, M. Carras, G. Isella, and D. Marris-Morini, Opt. Lett. **42**, 105 (2017).
17. V. Vakarin, J. M. Ramirez, J. Frigerio, Q. Liu, A. Ballabio, X. Le Roux, C. Alonso-Ramos, G. Isella, P. Cheben, W. N. Ye, L. Vivien, and D. Marris-Morini, Appl. Sci. **8**, 1154 (2018).
18. V. Vakarin, J. M. Ramirez, J. Frigerio, A. Ballabio, X. Le Roux, Q. Liu, D. Bouville, L. Vivien, G. Isella, and D. Marris-Morini, Opt. Lett. **42**, 3482 (2017).
19. Q. Liu, J. M. Ramirez, V. Vakarin, X. Le Roux, C. Alonso-Ramos, J. Frigerio, A. Ballabio, E. Talamas Simola, D. Bouville, L. Vivien, G. Isella, and D. Marris-Morini, Opt. Lett. **43**, 5021 (2018).
20. Q. Liu, J. M. Ramirez, V. Vakarin, X. Le Roux, J. Frigerio, A. Ballabio, E. Talamas Simola, C. Alonso-Ramos, D. Benedikovic, D. Bouville, L. Vivien, G. Isella, and D. Marris-Morini, accepted in Opt. Express.
21. Q. Liu, J. M. Ramirez, V. Vakarin, X. Le Roux, A. Ballabio, J. Frigerio, D. Chrastina, G. Isella, D. Bouville, L. Vivien, C. Alonso-Ramos, and D. Marris-Morini, Opt. Mater. Express **8**, 1305 (2018).
22. W. Bogaerts, P. D. Heyn, T. V. Vaerenbergh, K. D. Vos, S. K. Selvaraja, T. Claes, P. Dumon, P. Bienstman, D. V. Thoughout, and R. Baets, Laser Photon. Rev. **6**, 47 (2012).
23. Z. Cheng, X. Chen, C. Y. Wong, K. Xu, and H. K. Tsang, IEEE Photon. J. **4**, 1510 (2012).
24. R. Shankar, I. Bulu, and M. Lončar, Appl. Phys. Lett. **102**, 051108 (2013).
25. A. G. Griffith, R. K. Lau, J. Cardenas, Y. Okawachi, A. Mohanty, R. Fain, Y. H. D. Lee, M. Yu, C. T. Phare, C. B. Poitras, A. L. Gaeta, and M. Lipson, Nat. Commun. **6**, 6299 (2015).
26. A. Spott, Y. Liu, T. Baehr-Jones, R. Ilic, and M. Hochberg, Appl. Phys. Lett. **97**, 213501 (2010).
27. A. E. J. Lim, J. Song, Q. Fang, C. Li, X. Tu, N. Duan, K. K. Chen, R. Poh-Cher, and T. Y. Liow, IEEE J. Sel. Top. Quantum Electron. **20**, 405 (2014).
28. C. Rosenblad, H. R. Deller, A. Dommann, T. Meyer, P. Schroeter, and H. J. Von Kaenel, J. Vac. Sci. Technol. A **16**, 2785 (1998).
29. J. M. Ramirez, Q. Liu, V. Vakarin, J. Frigerio, A. Ballabio, X. Le Roux, D. Bouville, L. Vivien, G. Isella, and D. Marris-Morini, Opt. Express **26**, 870 (2018).
30. F. Turri, F. Ramiro-Manzano, I. Carusotto, M. Ghulinyan, G. Pucker, and L. Pavesi, J. Lightwave Technol. **34**, 5385 (2016).